Imaging Dispersion of MASW Data—Full vs. Selective Offset Scheme

Choon B. Park
Park Seismic LLC, Shelton, Conn. 06484
Email: choon@parkseismic.com

ABSTRACT

The dispersion imaging scheme for multichannel surface waves involves summation of a given frequency component over all traces in one record, always including wavefields in the full-offset range in the calculation. The scheme, therefore, does not have any way to take into account near- and far-field effects of surface waves, especially far-field effects, which can result in degraded imaging performance because of low amplitudes in the image space. Far-field effects are caused by noise wavefields dominating at far offsets where source-generated surface waves become relatively weak because of attenuation and geometrical spreading. The adverse influence of far-field effects can be minimized by considering an optimum far offset, which may not be the same as the farthest offset surveyed, but shorter depending on the wavelength being considered. Because the surface wave attenuation is proportional to distance in wavelength, the optimum far offset can be set to a specific number of wavelengths. On the other hand, the geometrical spreading affects all wavelengths equally and this alleviates the need for any other elaborate scheme. In this study, a selective-offset scheme is presented that limits the minimum and maximum offsets used for the imaging to 0.1–1.0 and 3–7 times, respectively, the wavelengths considered. It is shown that a selective-offset scheme can result in dispersion images with improved details, especially at those points dealing with relatively short wavelengths that are vulnerable to attenuation. The common full-offset scheme is explained in more intuitive ways than previously presented and, by extending it, the selective-offset scheme is explained.

Introduction

Principles of dispersion imaging commonly used in the multichannel analysis of surface waves (MASW) method (Park *et al.,* 1999) are based on the summation of wavefields existing at all traces in one field record. The summation is repeated along many different linear slopes in time-offset domain that correspond to different phase velocities of plane-wave propagation. At the correct phase velocity of a frequency component being considered, the summation yields the largest amplitude through constructive interference, whereas it results in smaller or insignificant amplitudes at all other velocities through destructive interference. Dispersion images are recognized by patterns of these amplitude peaks occurring at consecutive frequencies. The method includes *w-p* (McMechan and Yedlin, 1981), *f-k* (Claerbout, 1985), and phase-shift (Park *et al.,* 1998) methods that are slightly different in the way the dispersion image is constructed. The phase-shift method is known to achieve the highest imaging resolution for a given offset range (Park *et al.,* 1998; Dal Moro *et al.,* 2003) and is currently the most popular in use among other two-dimensional (2-D) wavefield transformation methods. Regardless of the particular method used, each point in the image space—for example, a point of phase velocity c_0 at frequency f_0 in Fig. 1—is associated with a surface wave of a particular wavelength (λ_0); $\lambda_0 = c_0/f_0$. The calculation of amplitude at this point deals with summation of surface waves of wavelength λ_0 propagating at a phase velocity c_0. The summation takes wavefields in all traces of full-offset range used during data acquisition based on the assumption that the signal surface wave of plane-wave propagation is present in all traces. Two factors may interfere with this assumption: the near- and far-field effects (Park *et al.,* 1999).

The near-field effects represent unpredictable non-planar propagation of surface waves near the source point caused by an excessive stress-strain relationship (Richart *et al.,* 1970). They are usually known to be responsible for underestimated phase velocities of relatively long wavelengths (Gucunski and Woods, 1991; Ryden and Mooney, 2009; Yoon and Rix, 2009; Park and Carnevale, 2010). The near-field effects are often associated with the minimum distance required for surface waves to develop through the interference of

JEEG, March 2011, Volume 16, Issue 1, pp. 13–23

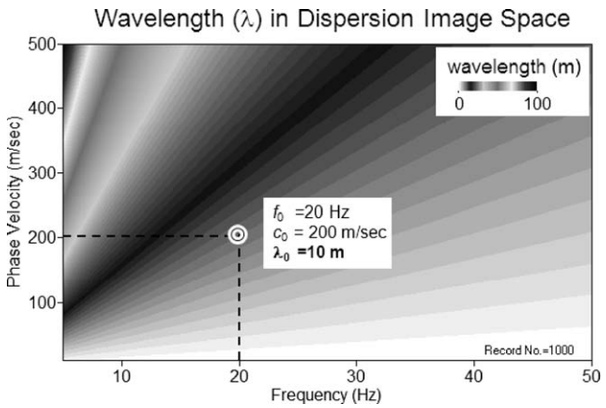

Figure 1. Different wavelengths (λ) associated with each point in dispersion imaging space with frequency (f) and phase velocity (c) axes. A particular point is indicated to show the relationship of λ = c/f.

multiple reflections and mode conversions of body (both P and S) waves at the free surface (Lamb, 1917; Viktorov, 1967). The optimum near offset, x_{near}, that minimizes these effects has been one of the most controversial topics in the traditional two-receiver approach (Stokoe *et al.,* 1994). Although different studies report different recommendations on x_{near}, a consensus is that x_{near} is dependent on wavelength (λ); $x_{near} = \xi_{near}\lambda$ with $0.1 \le \xi_{near} \le 1.0$ (O'Neill, 2005). However, it has been known that the effects are much less serious with the multichannel approach because of its intrinsic averaging property (Park *et al.,* 1999, 2002).

The far-field effects (Park *et al.,* 1999) indicate that signal surface waves become relatively weak at far offsets because of attenuation and geometrical spreading, and are contaminated by noise wavefields such as traffic noise, random ambient noise, scattered surface waves, and body waves. The contamination can also be caused by higher modes of surface waves that may prevail at far offsets because of their relatively smaller attenuation. If these contaminated wavefields are included in the summation operation of dispersion imaging, they tend to cause destructive interference even at the correct phase velocity of the frequency component being calculated, and hinder it from obtaining large amplitude in the image space. An optimum far offset, x_{far}, would be the maximum offset, which is smaller than (or equal to) the actual maximum offset of the record, to be included in the summation to minimize this adverse influence. It, however, should change with wavelength because the attenuation is a wavelength-dependent phenomenon (Johnston and Toksöz, 1981); $x_{far} = \xi_{far}\lambda$. The optimum value of ξ_{far} cannot be determined theoretically because subsurface attenuation properties (Q values) are not known beforehand. In addition, different seismic source power can influence the determination of optimum ξ_{far} differently. Thus, the optimum ξ_{far}value has to be determined empirically.

The selective-offset dispersion imaging (SODI) scheme presented here takes account of wavelength-dependent x_{far} and x_{near} in the summation operation. The commonly-used full-offset dispersion imaging (FODI) scheme in the original form introduced in Park *et al.* (1998) is reformulated so that it can be more intuitively understood. The SODI scheme is formulated by extending the FODI formulation. Comparative performance of both schemes is illustrated by using synthetic and real data sets.

Full-Offset Dispersion Imaging (FODI)

The dispersion imaging scheme most commonly adopted in the MASW method is described in discrete formulations. These formulations are more easily understood than the analytical descriptions presented in Park *et al.* (1998).

An *N*-channel record r_i (t) (i = 1, 2, …, N) is defined as a gather of N independent measurements called traces, acquired by using a linear array of N receivers starting from an offset x_1 with a common receiver spacing (dx), and with its frequency-domain representation of $R_i(\omega) = FFT[r_i]$ (i = 1, 2, …, N). $R_i(\omega)$ can be written as a product of the amplitude term, $A_i(\omega)$, and the phase term, $P_i(\omega)$: $R_i(\omega) = A_i(\omega)P_i(\omega)$. The amplitude term $A_i(\omega)$ changes with offset (x_i) and frequency (ω) because of spherical divergence, attenuation, and source spectrum characteristics. Conversely, the phase term $P_i(\omega)$ is determined only by the phase velocity (c_ω) of each frequency ω (=2πf) and offset (x_i):

$$P_i(\omega) = e^{-j\Phi_i(\omega)}, \text{ with } j = \sqrt{-1}, \quad (1)$$

where

$$\Phi_i(\omega) = 2\pi f \delta t = \omega x_i / c_\omega = \omega\{x_1 + (i-1)dx\}/c_\omega. \quad (2)$$

Consider one specific frequency (*e.g.,* 20 Hz) of surface waves, $R_i(\omega)$, recorded at offset x_i. Its time-domain representation will be a sinusoid curve whose amplitude and phase change with offset. Since the amplitude does not contain any information linked to phase velocity, $R_i(\omega)$ can be normalized to remove the effects of geometrical spreading and attenuation:

$$R_{i,norm}(\omega) = R_i(\omega)/|R_i(\omega)| = P_i(\omega). \quad (3)$$

This normalization helps the analysis to be focused on the phase velocity effect only (Park *et al.,* 1998). It also plays an important role in imaging relatively high frequency components of surface waves that could

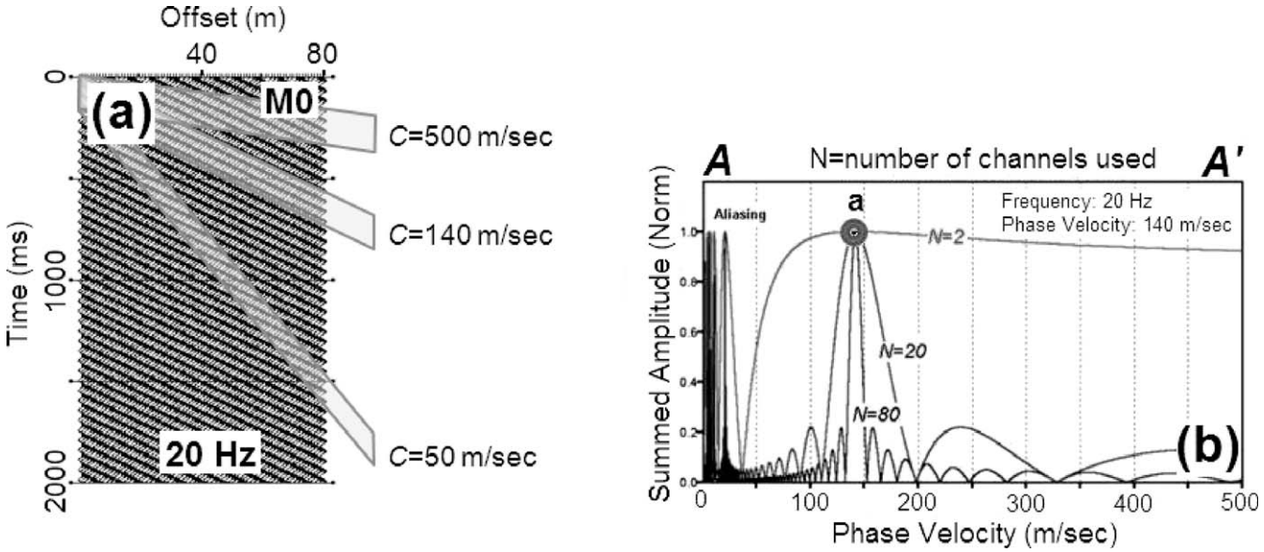

Figure 2. (a) A surface wave of an arbitrary frequency of 20 Hz with an arbitrary phase velocity of 140 m/s, and (b) curves of summed amplitudes for different numbers of traces (offset ranges).

otherwise be lost because of severely attenuated amplitudes at far-offset traces. Figure 2(a) shows an array of sinusoid curves of unit amplitudes for an arbitrary frequency of 20 Hz propagating at an arbitrary phase velocity of 140 m/s. It is noticed in the figure that sinusoid curves have the same phase along a slope (S_0) of the phase velocity, whereas they have a different phase along the slopes of other phase velocities. Therefore, if the curves are summed together within a finite time length (*e.g.,* one period) along the slope S_0, then it will give another sinusoid curve of amplitude $A_S = N$ through a perfectly constructive superposition. Conversely, A_S will be smaller than N if the summation is performed along other slopes because of a destructive superposition. This is the core concept of the slant-stack process (Claerbout, 1985) and is the key element of the dispersion imaging scheme. In practice the summation can be performed in a scanning manner along many different slopes specified by different phase velocities changing by small increments (*e.g.,* 5 m/s) within a broad range (*e.g.,* 10 m/s–1,500 m/s). The result of each summation, as represented by amplitude A_S of summed sinusoid curves, can be displayed in a 2-D format (*i.e.,* phase velocity versus A_S) (Fig. 2(b)). In this 2-D scanned curve, the phase velocity that gives the maximum amplitude ($A_{S,max}$) will be the correct value being sought. As illustrated in Fig. 2(b), the 2-D scanned curve has one main lobe with a peak amplitude $A_{S,max}$ and many side lobes on both sides. It is the sharpness of this main lobe that affects the resolution and accuracy of the analyzed dispersion relationship (Park *et al.,* 2001). In general, the sharpness of the peak increases with total length of the receiver array used in the summation (therefore, with N for a given dx). This effect is illustrated in Fig. 2(b) for N values of 2, 20, and 80 traces. The curves have been normalized with respect to N so that the peak value is unity in all three cases.

The aforementioned summation operation can be described in the frequency domain as follows:

$$\begin{aligned} A_s(c_T,\omega) &= \left(\frac{1}{N}\right)\sum_{i=1}^{N} e^{-j\delta_{i,T}} R_{i,norm}(\omega) \\ &= \left(\frac{1}{N}\right)\left[e^{-j\delta_{1,T}} R_{1,norm}(\omega) + e^{-j\delta_{2,T}} R_{2,norm}(\omega) \right. \\ &\qquad \left. + \cdots + e^{-j\delta_{N,T}} R_{N,norm}(\omega)\right] \end{aligned} \tag{4}$$

where

$$\delta_{i,T} = \omega x_i / c_T \text{ with } x_i = x_1 + (i-1)dx. \tag{5}$$

The expression in Eq. (5) is a phase shift uniquely determined by a testing phase velocity (c_T). $A_S(c_T, \omega)$ is a complex number whose absolute value ($|A_S(c_T, \omega)|$) is the same as the normalized amplitude (A_S) of the summed sinusoid wave of frequency ω previously explained in the time domain. Because of the normalization term in Eq. (4), the absolute value will be unity at $c_T = c_\omega$, whereas it will be less at all other values of c_T.

When seismic wave propagation invokes multimodal characteristics (*e.g.,* inclusion of higher modes) or includes different types of waves (*e.g.,* body and surface waves together), a multiple number of phase velocities can exist at the same frequency. This multi-phase-velocity case can be treated as a linear superposition of

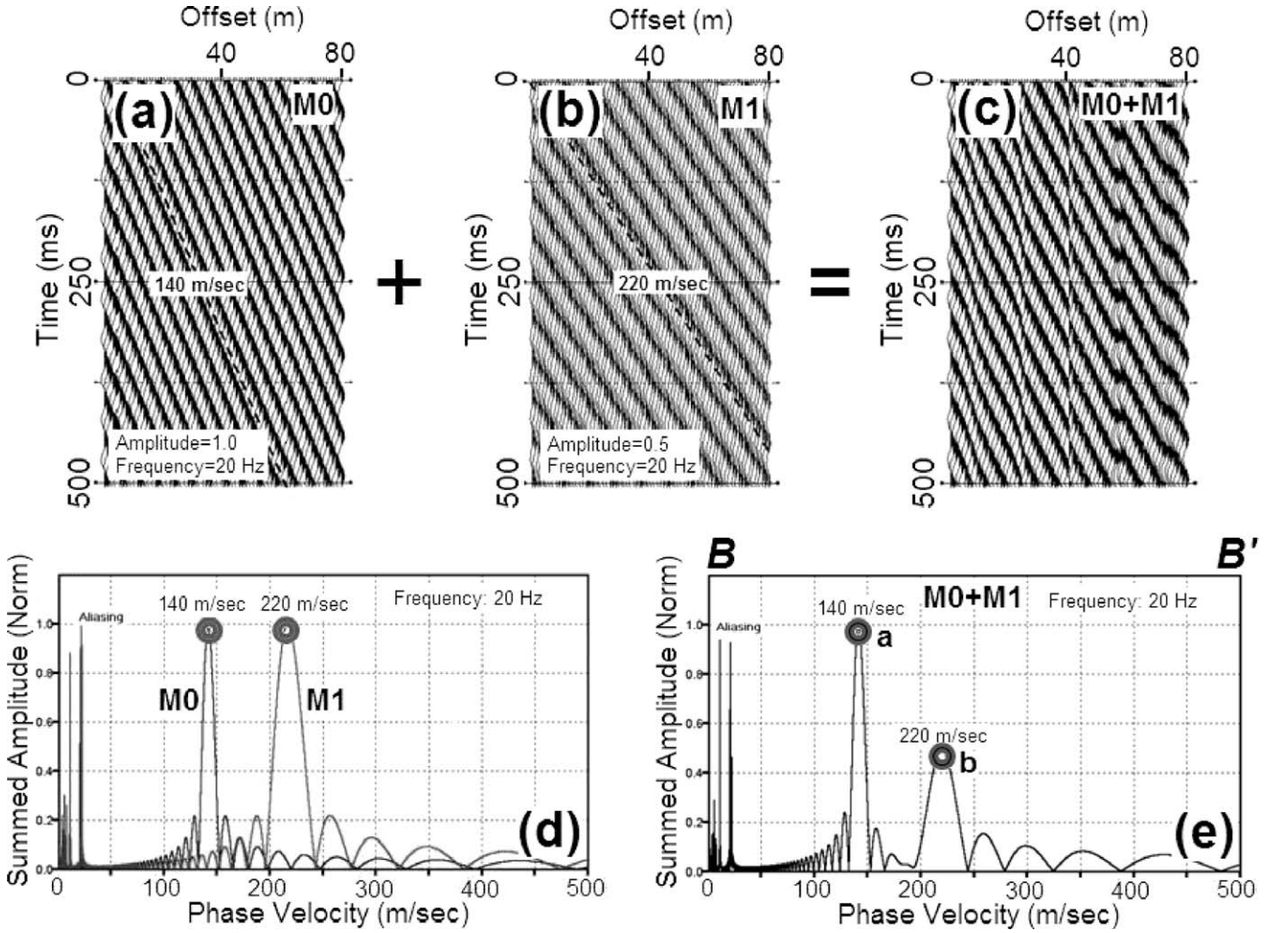

Figure 3. (a) 20-Hz surface wave component of the fundamental mode (M0), (b) the first higher mode (M1), and (c) sum of the two. Individual curves of summed amplitude for (a) and (b) are shown in (d), and the sum of these two curves is shown in (e).

individual single-phase-velocity cases. For example, if there exists a fundamental mode (M0) (Fig. 3(a)) and one higher mode (M1) (Fig. 3(b)) at the same frequency with different phase velocities, the measured wavefield then would be the same as a superposition (Fig. 3(c)) of the two separate records. This means that if the phase-velocity scanning is applied to this multi-modal record, the resulting scanned curve will be the same as a superposition (Fig. 3(e)) of the two individual scanned curves (Fig. 3(d)) obtained from each single-mode record. In this case, however, Park *et al.* (2001) indicate that the superposition involves a scaling term determined by the relative energy partitioning between the two modes. Therefore, two main lobes appear with different peak amplitudes. To identify dispersion trends over different frequencies, all 2-D curves at different frequencies are assembled into a three-dimensional (3-D) image showing the energy distribution as a function of phase velocity and frequency. Figure 4 shows modeling cases to illustrate the imaging principles for the single- and multi-modal cases. Further description of the modeling is presented in the later section of Synthetic Data.

Selective-Offset Dispersion Imaging (SODI)

As depicted by Eq. (4) in the previous section, the amplitude of a specific point in the image space is determined by a summation process that applies to all traces in the record (i = 1, …, N) regardless of the location of the point, taking into account the full-offset range used during data acquisition. The new scheme described in this section, however, applies the summation only to those traces in a selected offset range (*e.g.*, i = l_{near}, …, l_{far}) that changes with the wavelength (λ) of the point being calculated:

$$A_{s,SODI}(c_T,\omega)=\left(\frac{1}{l_{far}-l_{near}+1}\right)\sum_{i=l_{near}}^{l_{far}} e^{-j\delta_{i,T}}R_{i,norm}(\omega) \quad (6)$$

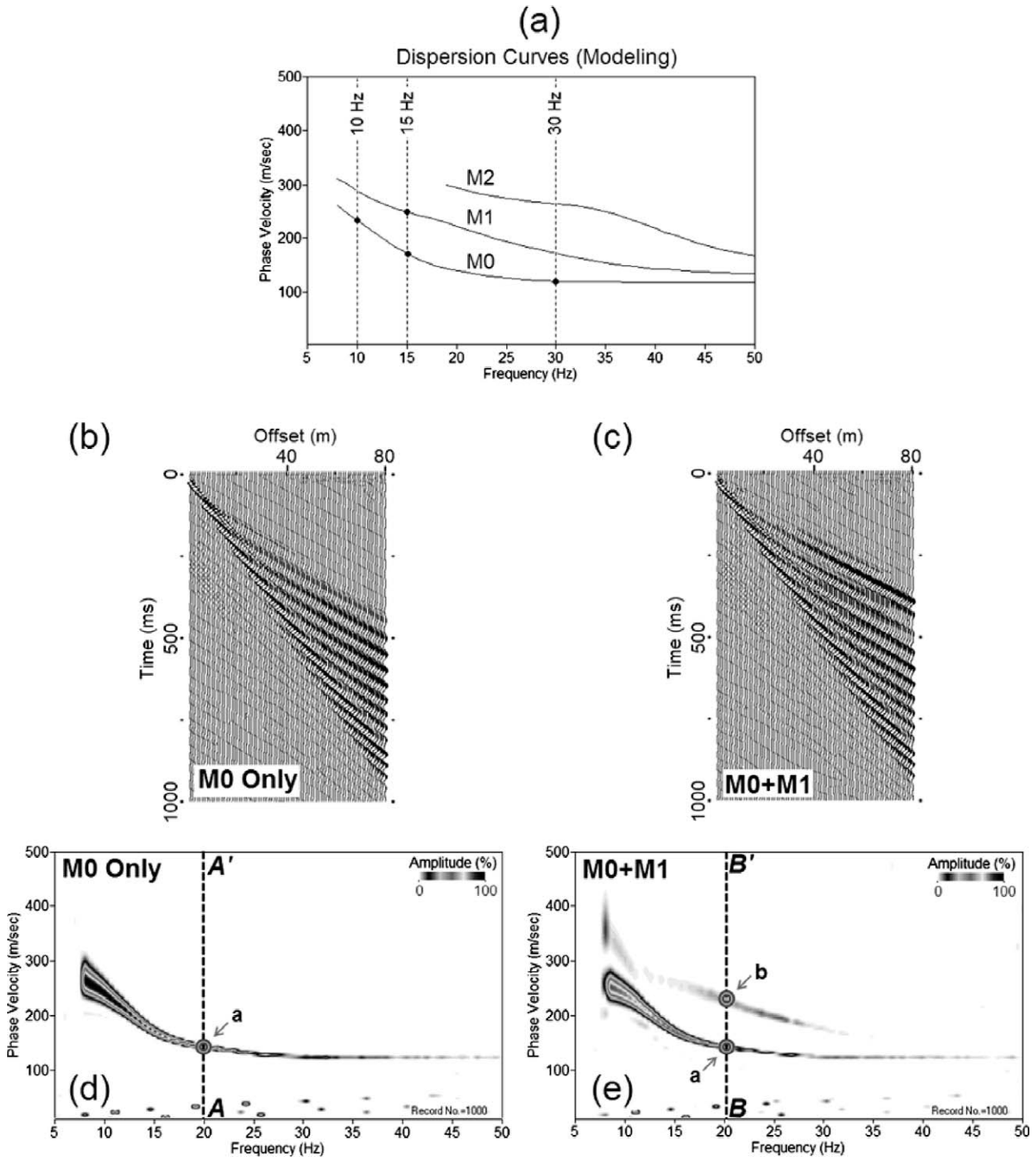

Figure 4. (a) Multimodal dispersion curves used to generate various types of synthetic data; two synthetic records containing one (b) and two (c) modes of surface waves and their corresponding dispersion images ((d) and (e), respectively). The lines A–A′ and B–B′ marked on these images are associated with the same lines indicated in Figs. 2(b) and 3(e), respectively.

where l_{near} and l_{far} are start and end indices, respectively, of traces falling in the selected offset range of $x_{near} \le x \le x_{far}$ satisfying the following relationship:

$$x_{near} = \xi_{near}\lambda, \text{ and } x_{far} = \xi_{far}\lambda \text{ where } \lambda = c_T/f. \quad (7)$$

Therefore, ξ_{near} and ξ_{far} determine minimum and maximum offsets for a given λ within which the summation has to take place. Their optimum values are determined in such a way that near- and far-field effects of surface waves, both of which are wavelength-

dependent phenomena, are best handled to minimize their adverse influence on the dispersion analysis. For a given λ, ξ_{near} determines the shortest distance free of the near-field effects (Park *et al.,* 1999; Park and Carnevale, 2010), whereas ξ_{far} determines the longest distance free of the far-field effects (Park *et al.,* 1999). Although different investigators in traditional surface wave methods using two receivers (Heasy *et al.,* 1982; Stokoe *et al.,* 1994) reported different criteria for ξ_{near} to avoid the near-field effects, they all fall in the following range (O'Neill, 2005):

$$0.1 \leq \xi_{near} \leq 1.0 \tag{8}$$

However, this range is not so critical with the multichannel approach because of the intrinsic property of the averaging effect (Park *et al.,* 1999, 2002).

The main motivation for selective offset processing as implied by Eq. (6), comes from the necessity to account for the far-field effects that are directly related to the attenuation of surface waves. On the other hand, effects of the geometrical spreading exert equally on all surface wave components and they can easily be accounted for, if deemed necessary, by physically removing relevant far-offset traces before processing with the full-offset scheme. The premise for the previous full-offset scheme is that a surface-wave component (ω) being processed exists throughout the entire offset range. This assumption holds true only if the propagating medium is perfectly elastic and noise free, and therefore the original energy ratio at generation time is preserved throughout the entire path of propagation. Most near-surface materials are far from this condition and surface waves inevitably lose their energy into heat energy as they propagate. This is the attenuation phenomenon, which is a wavelength-dependent process, as explained below.

The attenuation phenomenon is different from geometrical spreading, which depicts redistribution of total wave energy over an expanding area of the wavefront, and the phenomenon is usually expressed as an exponential loss of elastic energy with distance (Johnston and Toksöz, 1981):

$$A(x) = A_0 e^{-\alpha x}, \tag{9}$$

where $A(x)$ is the wave amplitude at distance x from the source, A_0 is the amplitude at the origin ($x = 0$), and α is the attenuation coefficient that determines how rapidly wave amplitude decreases with distance due to attenuation. α is determined by wave properties of frequency (f) and velocity (c), and an intrinsic medium property called quality factor (Q) (Johnston and Toksöz, 1981):

$$\alpha = \frac{\pi f}{cQ} = \frac{\pi}{\lambda Q} \tag{10}$$

Q is a ratio of stored energy to dissipated energy and a smaller Q means a more attenuating medium. Material with Q less than 10 are generally regarded as highly attenuating. According to Eq. (10), a shorter wavelength will suffer more from attenuation for a given distance x, and this effect will be compounded if the material is more attenuating (*i.e.,* a small Q). This means that at far offsets short wavelengths are more vulnerable to noise than long wavelengths. In this sense, the optimum far offset (x_{far}) should be determined as a ratio of wavelength (λ), not an absolute distance (x). This becomes more obvious if Eq. (9) is rearranged to calculate a distance x_μ where amplitude $A(x)$ drops to a certain ratio (μ) of its original value (*i.e.,* $\mu = A(x)/A_0 < 1.0$):

$$x_\mu = -\left(\frac{1}{\alpha}\right)\ln\mu = -\left[\left(\frac{Q}{\pi}\right)\ln\mu\right]\lambda = \xi\lambda, \tag{11}$$

where

$$\xi = -(Q/\pi)\ln\mu, \text{ and } \xi > 0.$$

ξ_{far} introduced in Eq. (7) is conceptually identical to an optimum value of ξ that determines the longest distance in λ from the source that a surface wave can travel without severe contamination by noise. A small value of ξ_{far} (*e.g.,* $\xi_{far} = 2$) indicates too few wavelengths are being included in the summation of Eq. (6), and this will result in thick-banded dispersion images jeopardizing modal separation (Park *et al.,* 2001). Likewise, a high value of ξ_{far} (*e.g.,* $\xi_{far} = 20$) will include too many wavelengths—including contaminated wavelengths at far offsets, making the selective-offset approach practically the same as the full-offset approach. It is also obvious that the more attenuating the materials are, the smaller ξ_{far} has to be. In addition, ξ_{far} can change even for a given Q because the trace distance (x) may also change with source offset (x_1) and receiver spacing (dx). Considering all these complications, ξ_{far} can be first determined through trial and error. However, from observations with diverse field data sets, any value in the following range is recommended:

$$3 \leq \xi_{far} \leq 7 \tag{12}$$

In fact, the following values of both ξ_{near} and ξ_{far} are recommended as the initial values during the trial-and-error determination of optimal values:

$$\xi_{near} = 0.5 \text{ and } \xi_{far} = 3.0 \tag{13}$$

Synthetic Data

To illustrate the comparative performance of full-offset (FODI) versus selective-offset (SODI) schemes previously described, synthetic records are generated by slightly modifying the algorithm introduced in Park and

Miller (2008). Although the algorithm was originally introduced to model passive MASW records, the main concept of generating a MASW record from given properties of dispersion and attenuation of surface waves is identical. The modified algorithm is briefly described below.

The i-th trace of the modeled record, $r_i(t)$, at offset $x_i = x_1 + (i-1)dx$ is obtained from the inverse FFT of its Fourier transformation, $R_i(\omega)$; $r_i(t) = FFT^{-1}[R_i(\omega)]$. Then, $R_i(\omega)$ is determined as

$$R_i(\omega) = \sum_{m=0}^{M} A_i^m P_i^m, \tag{14}$$

where A_i^m and P_i^m are amplitude and phase terms, respectively, for the m-th mode (0 = fundamental mode) of surface waves. These terms are determined by attenuation and dispersion properties, respectively, of surface waves as follows:

$$\begin{aligned} A_i^m &= A_0^m e^{-\alpha x_i} = A_0^m e^{-\omega x_i / (c_\omega^m Q)}, \\ P_i^m &= e^{j\omega(x_i / c_\omega^m)}, \end{aligned} \tag{15}$$

where A_0^m = amplitude of the m-th mode at the origin (x = 0), and c_ω^m = phase velocity of the m-th mode at frequency ω. Therefore, once all phase velocities are given by dispersion curves, the scheme accounts for attenuation and dispersion properties properly. It, however, does not consider near-field effects.

Two synthetic records are generated (Figs. 5(a)–(b)) according to the scheme of Eq. (14) by using all three modes of dispersion curves shown in Fig. 4(a). They represent results from all the same modeling parameters of frequency and offset ranges, and dispersion curves except for different Q's used (10 and 5, respectively) for the purpose of illustrating the relative sensitivity of the two schemes (FODI and SODI) to the attenuation. A relatively long offset range of 1–160 m was considered to emphasize the attenuation effects, and random noise of 5% total surface wave energy was included to simulate the far-field effects. However, it should be noted that random noise is not the only cause of the far-field effects and, in fact, ambient coherent noise such as traffic and scattered surface waves may often become dominating causes as well.

In Figs. 5(a)–(b), it is obvious that the record with a lower Q (=5) suffers more from the far-field effects. Figures 5(c)–(d) show dispersion images processed with the full-offset scheme (FODI). Both show that imaging quality degrades significantly as frequency (wavelength) becomes higher (shorter), especially in the case of lower Q. This is because the scheme included all traces during the summation process of Eq. (4), even if those far-offset traces do not have any useful surface wavefields but noise. On the other hand, the selective-offset scheme (SODI) with $\xi_{near} = 0.5$ and $\xi_{far} = 5.0$ results in dispersion images where all three modes are identified in almost the entire frequency range, as shown in Figs. 5(e)–(f). The improvement comes from SODI's ability to consider different optimum offset ranges for different wavelengths. This is further explained below by referring to the attenuation behavior of the four points marked on dispersion curves in Fig. 4(a).

Figure 6 considers the two points M0 and M1 at 15 Hz marked in Fig. 4(a). When attenuation is not so severe, with Q = 10 (Fig. 6(a)), both modes maintain their amplitudes above the noise level for almost two-thirds of the entire offset range. Therefore, the full-offset scheme could show relatively high amplitudes at the corresponding two image points in Fig. 5(c). However, when attenuation is severe, with Q = 5 (Fig. 6(b)), noise dominates over both modes for more than half the offset range. Consequently, the full-offset scheme did not show pronounced amplitudes at the two image points in Fig. 5(d). It should be noted that, although M0 possessed double the amplitude of M1 at generation time, it falls below the noise level more rapidly than M1. This is why the M0 point is less pronounced in the image. Offset ranges corresponding to $0.5\lambda \le x \le 5.0\lambda$ used in the selective-offset scheme (SODI) are indicated on top of each graph in Fig. 6, and show that the relative domination of noise becomes significantly reduced for both modes in each selected range.

Figure 7 considers three frequencies of 10 Hz, 15 Hz, and 30 Hz in the M0 curve indicated in Fig. 4(a). It is obvious that higher frequencies (shorter wavelengths) attenuate more rapidly than the lower frequencies (long wavelengths). In the less attenuating case of Q = 10 (Fig. 7(a)), the two lower frequencies of 10 Hz and 15 Hz have amplitudes above noise level for more than half the entire offset range; they could be imaged with pronounced amplitudes as seen in Fig. 5(c). The highest frequency of 30 Hz, however, attenuates so rapidly that its amplitude drops below the noise level for offsets greater than 40 m. This causes almost unnoticeable amplitude at the corresponding image point in Fig. 5(c). When the medium becomes more attenuating with Q = 5 (Fig. 7(b)), the 15 Hz component also falls below the noise level for most offsets and, therefore, its corresponding image point shows a barely noticeable amplitude as seen in Fig. 5(d). When only those selected offsets of $0.5\lambda \le x \le 5.0\lambda$, indicated on top of each graph in Figs. 7(a)–(b), are used for dispersion imaging with the selective offset scheme (SODI), the relative offset ratio of surface wave domination over noise becomes significantly increased for all three frequencies. This optimization of offset ranges for different wavelengths resulted in improved dispersion images as shown in Figs. 5(e)–(f).

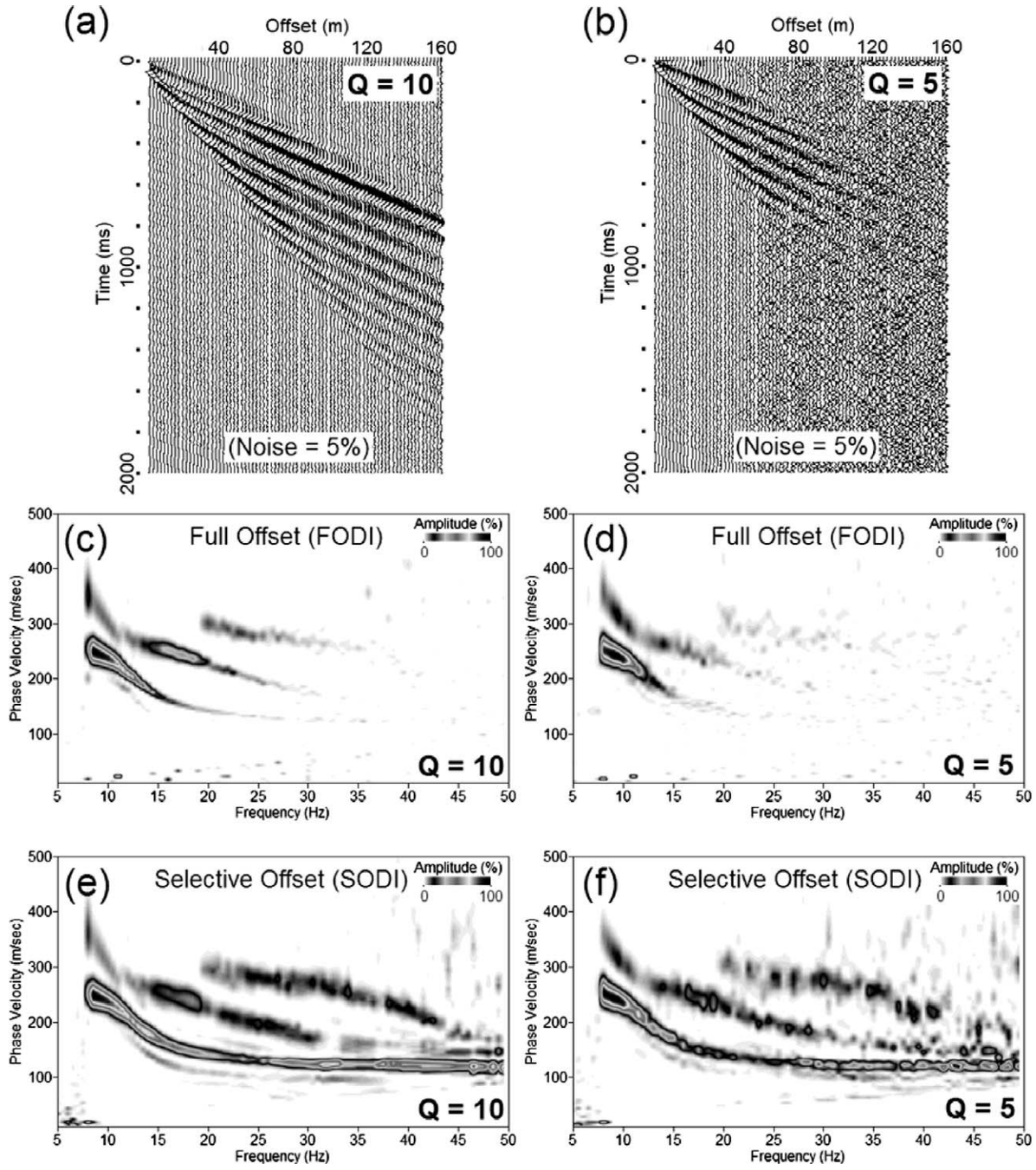

Figure 5. Synthetic records modeled by using Q = 10 (a) and Q = 5 (b) with 5% random noise. Corresponding dispersion images processed with full-offset (FODI), (c) and (d), and selective-offset (SODI), (e) and (f), schemes.

Field Data

Five field records are selected to illustrate the comparative performance of full-offset (FODI) versus selective-offset (SODI) schemes. Resulting images are shown in Fig. 8. These data sets are chosen from field records acquired during MASW surveys for wind-turbine site characterization (Park and Miller, 2005) at five locations in Oklahoma (Fig. 8(a)), New Mexico (Figs. 8(b)–(c)), and West Texas (Figs. 8(d)–(e)). All five sites consisted of relatively thin (or little) surficial soil underlain by weathered bedrock. The selective offset

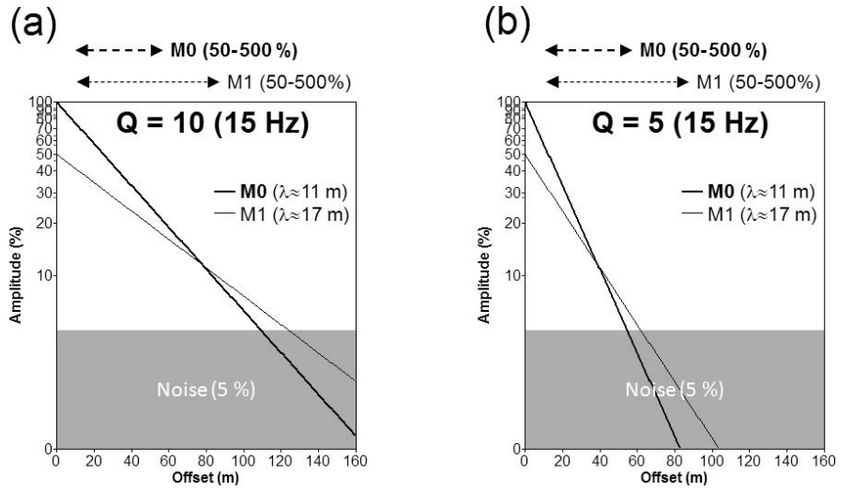

Figure 6. Amplitude curves changing with offset due to attenuation for the two surface wave components of M0 and M1 at 15 Hz marked in Fig. 4(a) in the cases of Q = 10 (a) and Q = 5 (b).

scheme, which used the offset range of $0.5\lambda \leq x \leq 5.0\lambda$, results in dispersion images of greater detail, especially at those regions of image space corresponding to relatively shorter wavelengths. This facilitates the interpretation of modal identities with observed dispersion patterns. These dispersion images are better suited for multi-mode inversion and have the advantage of increased investigation depth and overall accuracy (Xia *et al.,* 2000; Ernst, 2008; Casto *et al.,* 2010). Interpreted modal curves of fundamental (M0) and first higher (M1) modes have been superimposed in the images. Blank areas in the image (for example, the fan-shaped area at the bottom) indicate that no traces were available for the summation operation in the corresponding offset ranges.

Discussion

The role of the near-offset coefficient ξ_{near} is not as sensitive to imaging performance within the suggested range of $0.1 \leq \xi_{near} \leq 1.0$ as is the far-field coefficient ξ_{far}. In addition, the near-field effects are usually accounted for during data acquisition by optimum source offset (x_1) that is a certain ratio of total receiver spread length (L); for example, $x_1 \geq 0.5L$ (Park *et al.,* 1999; Park *et al.,* 2002; Ryden and Mooney, 2009; Yoon and Rix, 2009).

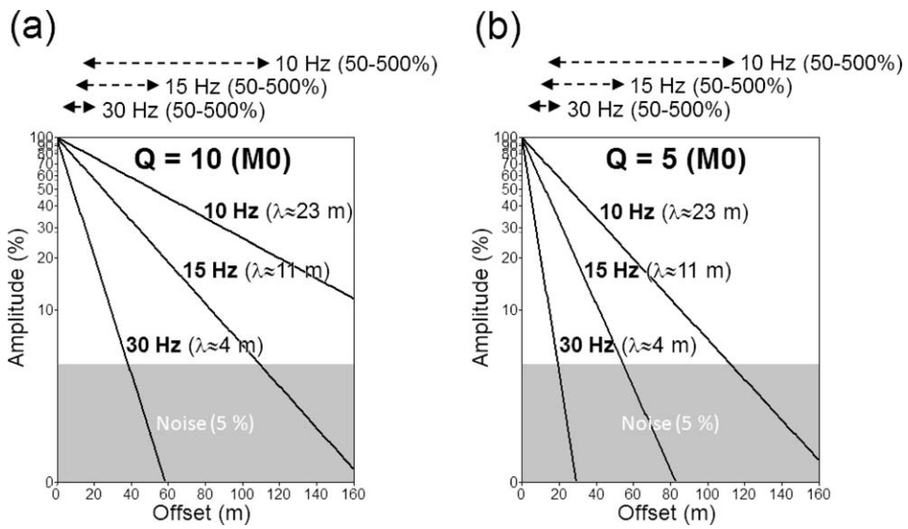

Figure 7. Amplitude curves changing with offset due to attenuation for the three surface wave components of M0 at 10 Hz, 15 Hz, and 30 Hz marked in Fig. 4(a) in the cases of Q = 10 (a) and Q = 5 (b).

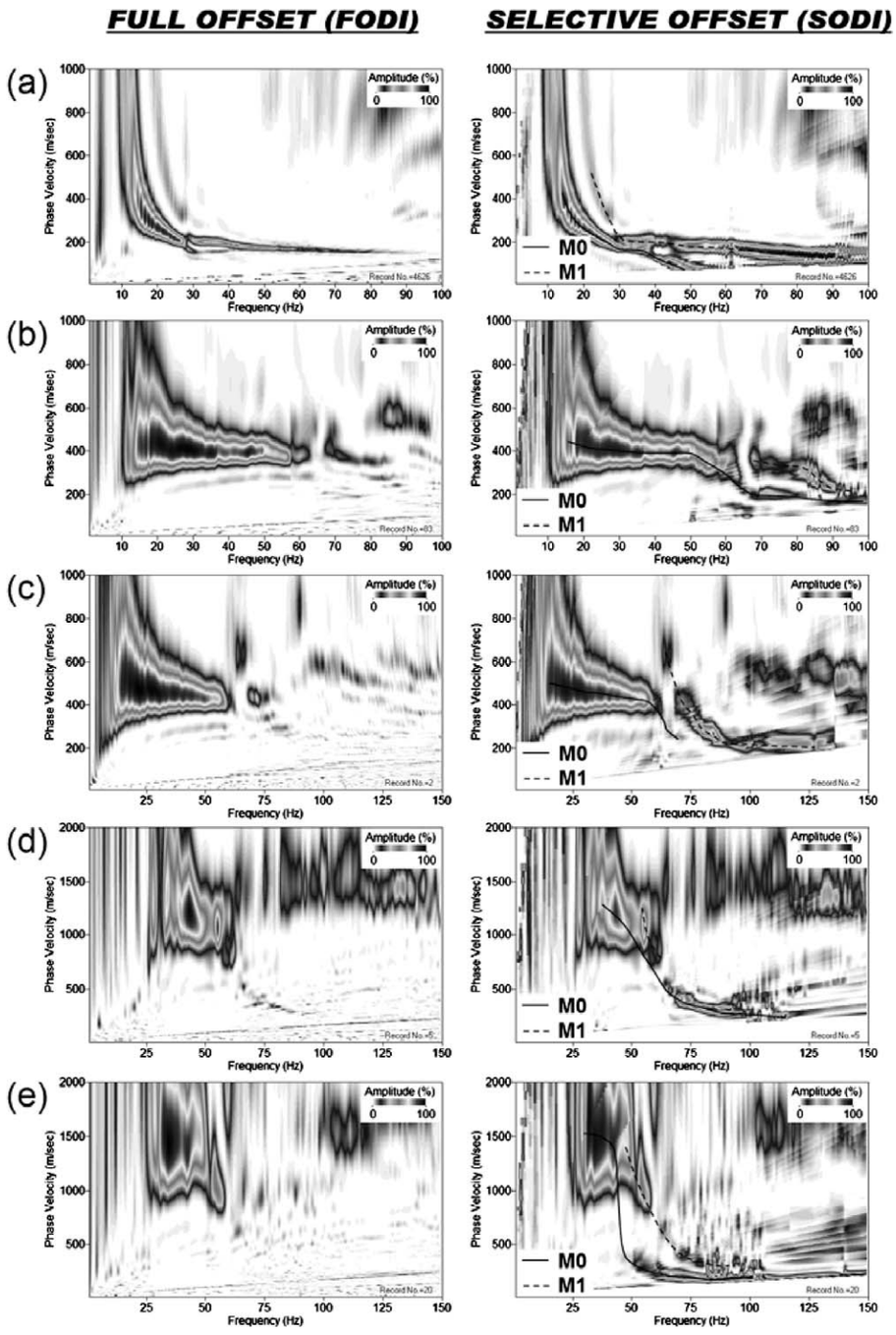

Figure 8. Dispersion images processed with full-offset (FODI) (left column) and selective-offset (SODI) (right column) schemes from field records acquired during the wind-turbine site characterizations in Oklahoma (a), New Mexico (b and c), and West Texas (d and e).

Although a range of values have been suggested for ξ_{far}, testing with several different values for a given data set is always recommended to find the optimal value. Tests with an increment of half wavelength (0.5λ) will be usually sufficient for this process. Therefore, the first step of a practical approach would be to pick an arbitrary value of ξ_{near} (for example, 0.5). Then, subsequent tests with an increment of 0.5 for ξ_{far} would be appropriate; for

example, a sequence with $0.5\lambda \le x \le 3.0\lambda$, $0.5\lambda \le x \le 3.5\lambda$, $0.5\lambda \le x \le 4.0\lambda$, …, $0.5\lambda \le x \le 7.0\lambda$.

The *f-k* method can also incorporate the selective-offset scheme into its transformation over wavenumber (*k*) direction. However, the scheme cannot be implemented with the *w-p* method by McMechan and Yedlin (1981) because it does not have a step that can selectively apply different offsets to the wavefield transformation process.

Conclusions

Commonly used full-offset dispersion imaging (FODI) schemes to process MASW field data, such as *w-p*, *f-k*, and phase-shift methods, involve summation of wavefields in all constituent traces of one field record. This can result in images adversely influenced by near- and far-field effects of surface waves, especially by the far-field effects.

The selective-offset dispersion imaging (SODI) scheme, constructed by modifying the phase-shift method, can account for wavelength-dependent phenomena of near- and far-field effects. This can result in dispersion images with enhanced clarity, especially at those imaging points dealing with relatively short wavelengths that are vulnerable to the far-field effects of severe attenuation. This in turn can help better delineate multi-modal characteristics of surface waves that have the potential to increase the investigation depth and the overall accuracy of the inversion process in search of the shear-velocity model. Empirically suggested values for an optimum offset (x) range for SODI is $\xi_{near}\lambda \le x \le \xi_{far}\lambda$ with $0.1 \le \xi_{near} \le 1.0$ and $3 \le \xi_{far} \le 7$.

References

Casto, D.W., Calderón-Macíasm, C., Luke, B., and Kaufmann, R., 2010, Improving MASW results for a site with shallow bedrock through the use of higher-mode data: *in* Proceedings of GeoFlorida 2010.

Claerbout, J.F., 1985. Fundamentals of geophysical data processing: Blackwell Scientific Publications, Palo Alto, California, 274 pp.

Dal Moro, G., Pipan, M., Forte, E., and Finnetti, I., 2003, Determination of Rayleigh wave dispersion curves for near surface applications in unconsolidated sediments: *in* Expanded Abstracts: Society of Exploration Geophysicists, 1247–1250.

Ernst, F.E., 2008, Multi-mode inversion for P-wave velocity and thick near-surface layers: Proceedings in Near Surface 2008–14th European Meeting of Environmental and Engineering Geophysics.

Gucunski, N., and Woods, R.D., 1991, Instrumentation for SASW testing: *in* Bhatia, S.K., and Blaney, G.W. (eds.), Recent Advances in Instrumentation, Data Acquisition and Testing in Soil Dynamics: Am. Soc. Civil Eng., 1–16.

Heisey, J.S., Stokoe II., K.H., and Meyer, A.H., 1982, Moduli of pavement systems from Spectral Analysis of Surface Waves: Transp. Res. Rec., **852**, Washington D.C., 22–31.

Johnston, D.H., and Toksöz, M.N., 1981, Definitions and terminology: *in* Toksöz, M.N., and Johnston, D.H. (eds.), Seismic wave attenuation. SEG Geophysics reprint series, no. 2, 1–5.

Lamb, H., 1917. On waves in an elastic plate, Proceedings of the Royal Society, London, 114–128.

McMechan, G.A., and Yedlin, M.J., 1981, Analysis of dispersive waves by wave field transformation: Geophysics, **46**, 869–874.

O'Neill, A., 2005, Seismic surface waves special issue guest editorial: Journal of Environmental and Engineering Geophysics, **10**(2) 67–86.

Park, C.B., and Carnevale, M., 2010, Optimum MASW survey–revisit after a decade of use: *in* Proceedings of GeoFlorida 2010.

Park, C.B., and Miller, R.D., 2005, Seismic characterization of wind turbine sites near Lawton, Oklahoma, by the MASW method: Kansas Geological Survey Open-file Report 2005-22.

Park, C.B., and Miller, R.D., 2008, Roadside passive multichannel analysis of surface waves (MASW): Journal of Environmental and Engineering Geophysics, **13**(1) 1–11.

Park, C.B., Miller, R.D., and Miura, H., 2002, Optimum field parameters of an MASW survey: *in* Expanded Abstracts: Society of Exploration Geophysicists-Japan.

Park, C.B., Miller, R.D., and Xia, J., 1998, Imaging dispersion curves of surface waves on multi-channel record: *in* Expanded Abstracts: Society of Exploration Geophysicists, 1377–1380.

Park, C.B., Miller, R.D., and Xia, J., 1999, Multichannel analysis of surface waves (MASW): Geophysics, **64**, 800–808.

Park, C.B., Miller, R.D., and Xia, J., 2001, Offset and resolution of dispersion curve in multichannel analysis of surface waves (MASW): *in* Proceedings of the Symposium on the Application of Geophysics to Engineering and Environmental Problems, SSM-4.

Richart, F.E., Hall, J.R., and Woods, R.D., 1970. Vibrations of Soils and Foundations, Prentice-Hall, Inc.

Ryden, N., and Mooney, M., 2009, Analysis of surface waves from the light weight deflectometer: Soil Dynamics and Earthquake Engineering, **29**, 1134–1142.

Stokoe II., K.H., Wright, S.G., Bay, J.A., and Roësset, J.M., 1994, Characterization of geotechnical sites by SASW method: *in* Woods, R.D. (ed.), Geophysical Characterization of Sites, Oxford Publishers.

Viktorov, I.A., 1967. Rayleigh and Lamb waves, Plenum Press, New York.

Xia, J., Miller, R.D., and Park, C.B., 2000, Advantages of calculating shear-wave velocity from surface waves with higher modes: *in* Expanded Abstracts: Society of Exploration Geophysicists, 1295–1298.

Yoon, S., and Rix, G.J., 2009, Near-field effects on array-based surface wave methods with active sources: J. Geotech. Geoenviron. Eng., **135**(3) 399–406.